

# X-ray Microspectroscopy and Ptychography on Nanoscale Structures in Rock Varnish

Jan-David Förster,\* Iuliia Bykova, Dorothea S. Macholdt, Klaus Peter Jochum, Michael Kappl, A. L. David Kilcoyne, Maren Müller, Antje Sorowka, Bettina Weber, Markus Weigand, Gisela Schütz, Meinrat O. Andreae, and Christopher Pöhlker\*

Cite This: *J. Phys. Chem. C* 2021, 125, 22684–22697

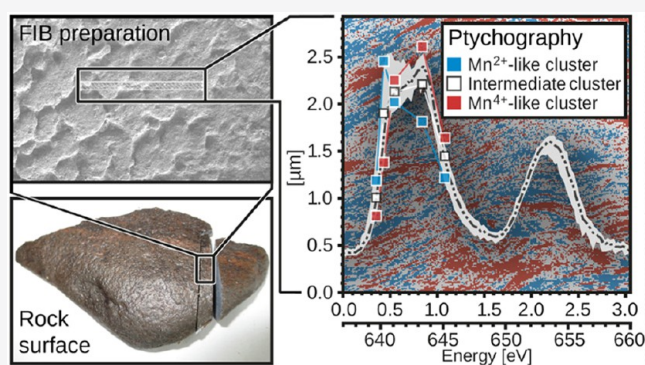
Read Online

ACCESS |

Metrics & More

Article Recommendations

**ABSTRACT:** X-ray microspectroscopy is a powerful analytical method in geoscientific and environmental research as it provides a unique combination of nanoscale imaging with high spectroscopic sensitivity at relatively low beam-related sample damage. In this study, “classical” scanning transmission soft X-ray microscopy (STXM) with X-ray absorption spectroscopy and the recently established soft X-ray ptychography are applied to the analysis of selected rock varnish samples from urban and arid desert environments. X-ray ptychography enhances the spatial resolution relative to STXM by up to 1 order of magnitude. With its high chemical sensitivity, it can resolve nanoscale differences in valence states of the key varnish elements manganese (Mn) and iron. Our results emphasize the complex nanoarchitecture of rock varnish as well as the diverse mineralogy of the Mn oxy–hydroxide matrix and its embedded dust grains. In contrast to the fast-growing urban varnish, the slow-growing arid desert varnish revealed a remarkable nanoscale stratification of alternating Mn valence states, providing hints on the layer-wise and still enigmatic growth process.



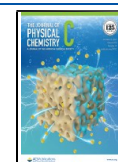
## INTRODUCTION

Microspectroscopic techniques, providing spectroscopic information at micrometer ( $\mu\text{m}$ ) or even nanometer (nm) scales have become essential tools in environmental research, geoscience, material science, and related scientific fields.<sup>1–3</sup> A widely used technique is scanning transmission X-ray microscopy (STXM) in combination with near-edge X-ray absorption fine structure (NEXAFS) analysis.<sup>4,5</sup> The analytical strength of STXM-NEXAFS is defined by its microscopic resolution in the few hundreds of nanometers range (with respect to resolved features), its high chemical sensitivity and rich spectroscopic information, as well as a relatively low beam-related sample damage.<sup>6–8</sup> A further development of STXM-NEXAFS is X-ray ptychography—the X-ray microscopic technique with the highest spatial resolution currently available.<sup>9,10</sup> X-ray ptychography combines STXM with diffraction imaging and subsequent reconstruction of the images.<sup>11–13</sup> Ptychography has been applied, e.g., in material science using either the soft or hard X-ray range and requires chemical, magnetic, or bond orientation contrast in the samples.<sup>9,10,14–17</sup> It provides images of extended sample areas with sub-10 nm resolution (with respect to resolved features) and, therefore, increases the resolution of “classical” STXM by about 1 order of magnitude.<sup>9,10</sup> The spatial

resolution is limited by diffraction rather than by the X-ray optics and is, thus, in principle wavelength-limited.

Microspectroscopy has been increasingly used in the analysis of rock varnish, a geological sample type whose properties and genesis have remained enigmatic since its first description by Alexander von Humboldt and Aimé Bonpland (1819).<sup>18</sup> Rock varnishes are naturally occurring, up to few hundred micrometers thin and hard black or brownish layers that primarily consist of poorly crystallized manganese (Mn) and iron (Fe) oxides and hydroxides (5–20%)—shortly noted as oxy–hydroxides—that cement together clay mineral grains (on average 60%) of airborne origin.<sup>19–24</sup> Rock varnishes have been described from quite different environments, such as arid and semiarid deserts,<sup>25–27</sup> for which the formation process is typically very slow (i.e., 1–40  $\mu\text{m}$  per 1000 years), river splash zones,<sup>28</sup> on buildings in urban locations,<sup>29</sup> and presumably also at extraterrestrial sites.<sup>23,30,31</sup> Up to now, the potential

Received: April 21, 2021  
Revised: August 16, 2021  
Published: October 6, 2021



mechanisms that control the precipitation of the varnish layers on rock surfaces have been discussed controversially: On the one hand, abiotic formation models suggest that thermodynamic and kinetic characteristics of leaching and reprecipitation equilibria of certain elements (i.e., Mn, Fe, Si, etc.) suffice to explain the formation process.<sup>25,32–34</sup> On the other hand, biotic formation models advocate that Mn-oxidizing microorganisms play key roles in varnish formation and, therefore, have to be considered to explain the observations.<sup>35–38</sup> The jury is still out on varnish genesis, which keeps inspiring researchers to apply cutting-edge techniques to solve this “old mystery”.

Microscopic analyses have provided insights into  $\mu\text{m}$  as well as nm structures inside the varnish. On micrometer scales, light microscopy on thin sections is widely used to determine the thickness and sequence of darker Mn-rich versus brighter Mn-poor microlaminations that are discussed as potential climate archives to reflect past millennia-scale climate conditions.<sup>25,39–41</sup> Furthermore, high-resolution scanning and transmission electron microscopy (SEM and TEM) applied to sections of varnish samples have provided even more detailed insights, indicating a high degree of complexity on nm scales.<sup>41–43</sup> In combination with energy-dispersive X-ray spectroscopy or electron energy-loss spectroscopy, SEM and TEM also provide chemical contrast, helping to determine element distributions and mineralogical identities.<sup>44–46</sup>

In our previous studies on rock varnish samples from various locations worldwide,<sup>8,47–49</sup> we applied STXM-NEXAFS (in combination with other techniques) to resolve the varnish micro- and nanoarchitecture with the finest detected features of varnish-relevant elements down to 100 nm. These analyses required focused ion beam (FIB) milling of ultrathin slices to allow microscopy in transmission mode. For the analysis of the chemical identity and bonding environment of 2p and 3d elements in rock varnish, the high chemical sensitivity of NEXAFS spectroscopy has proven to be particularly powerful.

Here, we applied X-ray ptychography to the analysis of the Mn and Fe  $L_{3,2}$  as well as the Al K absorption edges in selected rock varnish samples, providing highly resolved and chemically sensitive maps and, thus, unprecedented insights into the varnish nanostructures. As a key aspect, this analysis resolves the spectroscopic fine structure and its variability at the Mn  $L_{3,2}$  absorption edge, revealing the nanoscale differences in rock varnish geochemistry. This study represents one of the first applications of X-ray ptychography in geoscience,<sup>50,51</sup> and its results are embedded into a wider context of STXM-NEXAFS data, which demonstrates the analytical scope and particular strengths of ptychography for the analysis of geological as well as other environmental samples.

## MATERIALS AND METHODS

**Rock Varnish Samples.** From more than 20 rock varnish samples analyzed in our previous studies,<sup>8,47–49</sup> the following three samples were selected here for in-depth investigation by STXM-NEXAFS and/or X-ray ptychography:

- Sample SC is an urban varnish sample, collected from the facade of the Smithsonian Castle in Washington, DC. It belongs to the type IV varnish category, according to Macholdt et al.<sup>49</sup> A detailed description of the SC varnish can be found in Vicenzi et al.<sup>29</sup> and Sharps et al.<sup>52</sup> This sample was analyzed comprehensively by STXM-NEXAFS (through high-resolution

maps and spectra spanning various element absorption edges), and the corresponding data serves as an STXM-NEXAFS reference case and context in this study. Sample SC was not a subject of the X-ray ptychography analysis.

- Sample CA WS18 is an arid desert varnish sample, collected in Death Valley, CA. It belongs to the type I varnish category, according to Macholdt et al.<sup>49</sup> Further details can be found in Macholdt et al.<sup>47,49</sup> and Liu and Broecker.<sup>53</sup> This sample was selected for ptychography analysis because of its distinct Mn and Fe laminar microstructures.
- Sample CA14 JC8 is an arid desert varnish sample, collected in Death Valley (Johnson Canyon), CA. It belongs to the type I varnish category, according to Macholdt et al.<sup>49</sup> Further details can be found in Macholdt et al.<sup>47,49</sup> This sample was selected for ptychography analysis because of its distinct Mn and Fe microstructure.

**Focused Ion Beam Preparation.** Sample preparation of the varnish samples was conducted using the FIB lift-out technique. This technique allows a relatively fast and relatively contamination-free preparation and a precise selection of the target area.<sup>54,55</sup> It was performed at the Max Planck Institute for Polymer Research, Mainz, Germany, using a Nova 600 Nanolab FIB dual-beam instrument from FEI (Hillsboro, OR). Simultaneously, SEM observation was conducted to determine and monitor the site of milling (5 kV acceleration voltage). Prior to the transfer to the FIB instrument, the samples were sputtered with 50 nm of platinum (Pt) to minimize sample charging during SEM imaging and FIB milling. After additional FIB-induced deposition of a 2–3  $\mu\text{m}$  thick protective Pt stripe ( $50 \times 3 \mu\text{m}^2$ ) from a metallo-organic precursor gas, milling was performed by gallium-ion ( $\text{Ga}^+$ ) sputtering with a resolution of about 10 nm. At the end of the preparation procedure, which involves multiple cutting and polishing steps, previously described elsewhere in greater detail,<sup>8</sup> wedge-shaped, 30–40  $\mu\text{m}$  long lamellae with typical thicknesses between 80 nm at the top and about 1  $\mu\text{m}$  at the bottom were obtained. The wedge shape was chosen to improve the stability of the sample. These values were measured from SEM micrographs, some of which are shown in Figure 1. Details on sample preparation requirements as well as limitation of the sample preparation and analysis are critically discussed by Krinsley et al.<sup>56</sup> and Macholdt et al.,<sup>8</sup> respectively.

**STXM-NEXAFS Measurements and Data Analysis.** The STXM-NEXAFS data presented here were measured at two X-ray microscopes: (i) the MAXYMUS microscope at the undulator beamline UE46-PGM-2 at the synchrotron BESSY II, Helmholtz-Zentrum, Berlin, Germany, and (ii) the X-ray microscope at the bending magnet beamline 5.3.2.2 at the synchrotron Advanced Light Source (ALS), Lawrence Berkeley National Laboratory, USA. The BESSY II measurements were conducted in single-bunch top-up mode, whereas the ALS measurements were conducted in multibunch top-up mode. The ALS-STXM spans an energy range of 250–800 eV, covering the following varnish-relevant absorption edges: K-edge of carbon (C),  $L_{3,2}$ -edge of potassium (K),  $L_{3,2}$ -edge of calcium (Ca), K-edge of nitrogen (N),  $L_{3,2}$ -edge of titanium (Ti), K-edge of oxygen (O),  $L_{3,2}$ -edge of Mn, and  $L_{3,2}$ -edge of Fe. It provides an energy resolution of  $E/\Delta E \leq 5000$  at C.<sup>57</sup> The MAXYMUS-STXM spans an energy range of 270–1900

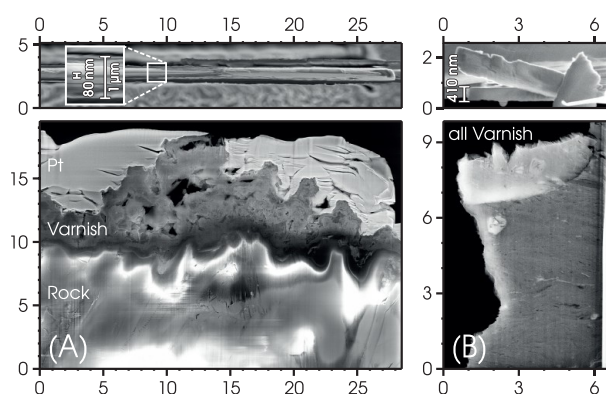


**Figure 1.** SEM micrographs of the wedge-shaped FIB slices of rock varnish samples SC (left column A) and CA WS18 (right column B) in the top view (top row) and front view (bottom row). The thickness of FIB slices typically ranges from 80 nm at the top to about 1  $\mu\text{m}$  at the bottom. Note that after the thinning of sample CA WS18, the slice broke apart and only its lower half was preserved. For this sample, the remaining varnish-containing protrusion is 410–430 nm thick. All axes in micrometers.

eV, covering all aforementioned absorption edges and in addition the  $L_{3,2}$ -edge of cobalt (Co),  $K$ -edge of sodium (Na),  $K$ -edge of aluminum (Al), and  $K$ -edge of silicon (Si). It provides a resolution of  $E/\Delta E \leq 8000$  at C.<sup>58,59</sup>

For energy calibration, polystyrene latex (PSL) spheres were measured and the characteristic  $\pi$  resonance peak of the phenyl moiety at 285.2 eV at the C edge was used for the correction of the spectra.<sup>60,61</sup> At the Mn and Fe  $L_{3,2}$ -edges, the energy calibration was validated by means of NEXAFS spectra of the reference compounds MnO,  $\text{Mn}_2\text{O}_3$ ,  $\text{MnO}_2$ ,  $\text{Fe}_3\text{O}_4$ , and  $\text{Fe}_2\text{O}_3$ . The STXM-NEXAFS data analysis was conducted using the

Multivariate Analysis Tool for Spectromicroscopy software (MANTiS-3.0.01)<sup>62–64</sup> and the Interactive Data Language (IDL) widget “Analysis of X-ray microscopy Images and Spectra” (aXis2000).<sup>65</sup> This included the extraction of spectra, the map creation and the cluster analysis (CA). FFT-prefiltering of the ptychographic reconstructions was done in Fiji/ImageJ 1.52a and 1.52n.<sup>66</sup> MANTiS compatible files were compiled from the filtered reconstructions via custom-made scripts, programmed in Python 3.6.5. Gwyddion-2.41 was used to extract line profiles from the microscopy data. Final analysis steps for the STXM-NEXAFS spectra were conducted in IGOR Pro (Wavemetrics, version 7.08, Lake Oswego, OR). The figure compositing was done in Adobe Illustrator CS6-16.0.3.

**Ptychography Measurements and Data Analysis.** The ptychography measurements were conducted at the MAXYMUS X-ray microscope at BESSY II (Berlin, Germany). Ptychographic images are produced by scanning a sample in raster mode with a certain degree of overlapping of neighboring illumination spots. During the scan, diffraction patterns are recorded in a far-field configuration by a charge-coupled device (CCD) detector. Phase and amplitude images are retrieved by an iterative algorithm using redundant diffraction data as the boundary condition. The Fresnel zone plate (FZP) used for ptychographic imaging was custom-made using ion beam lithography (IBL) at the Modern Magnetic Systems Department at the Max Planck Institute for Intelligent Systems, Stuttgart, Germany.<sup>67</sup> The FZP with a diameter of 120  $\mu\text{m}$  and an outermost zone width of 100 nm produces a 120 nm large focus spot that is estimated as full-width half-maximum (fwhm) of the illumination profile. The sample was scanned with a step size of 80 nm in raster mode, which resulted in more than 33% overlap of the neighboring regions.

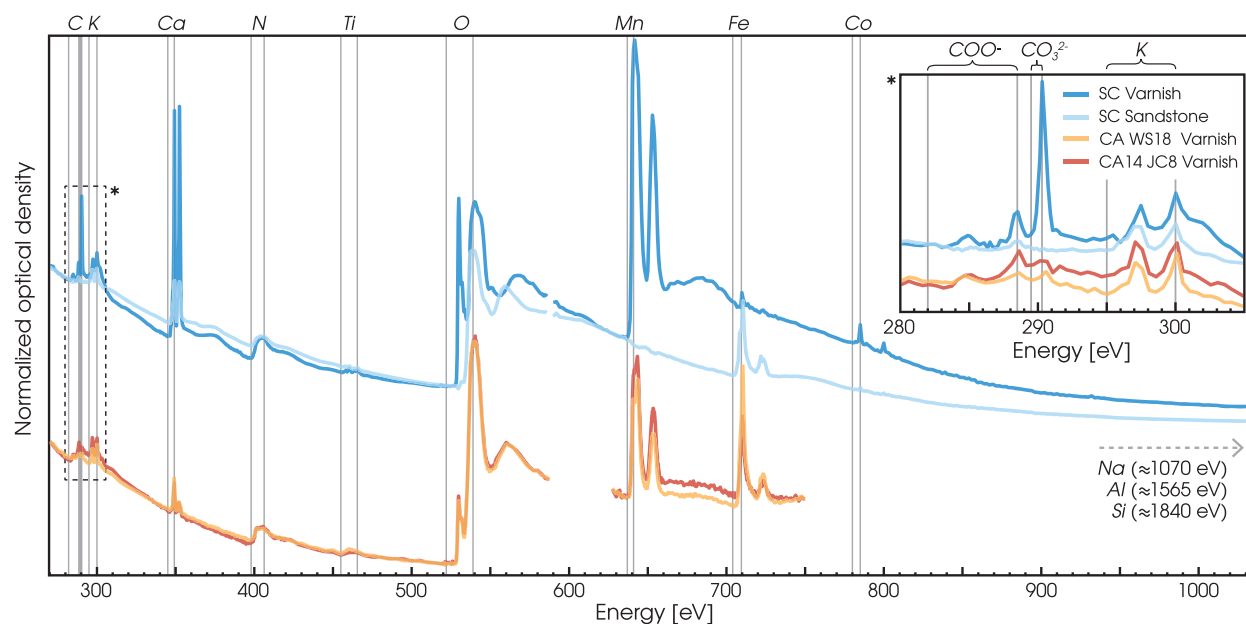


**Figure 2.** NEXAFS spectra covering multiple absorption edges for the varnish samples SC, CA WS18, and CA14 JC8. The spectra represent the average compositions of the varnish within the FIB slices. For sample SC, a corresponding spectrum of the underlying sandstone is shown as well. Sample SC was measured at the MAXYMUS-STXM, which provided a wide energy range (up to about 1900 eV). The samples CA WS18 and CA14 JC8 were measured at the ALS-STXM with a narrower energy range (up to about 800 eV). An artificial vertical spacing was inserted between the MAXYMUS and the ALS data to enhance the readability. The enlarged region (marked by an asterisk) emphasizes spectral details at the C edge for clarity, e.g., the  $\text{CO}_3^{2-}$  resonance at 290.3 eV. The vertical lines represent the energy value pairs at which the elemental and functional group maps in Figure 3 were recorded.

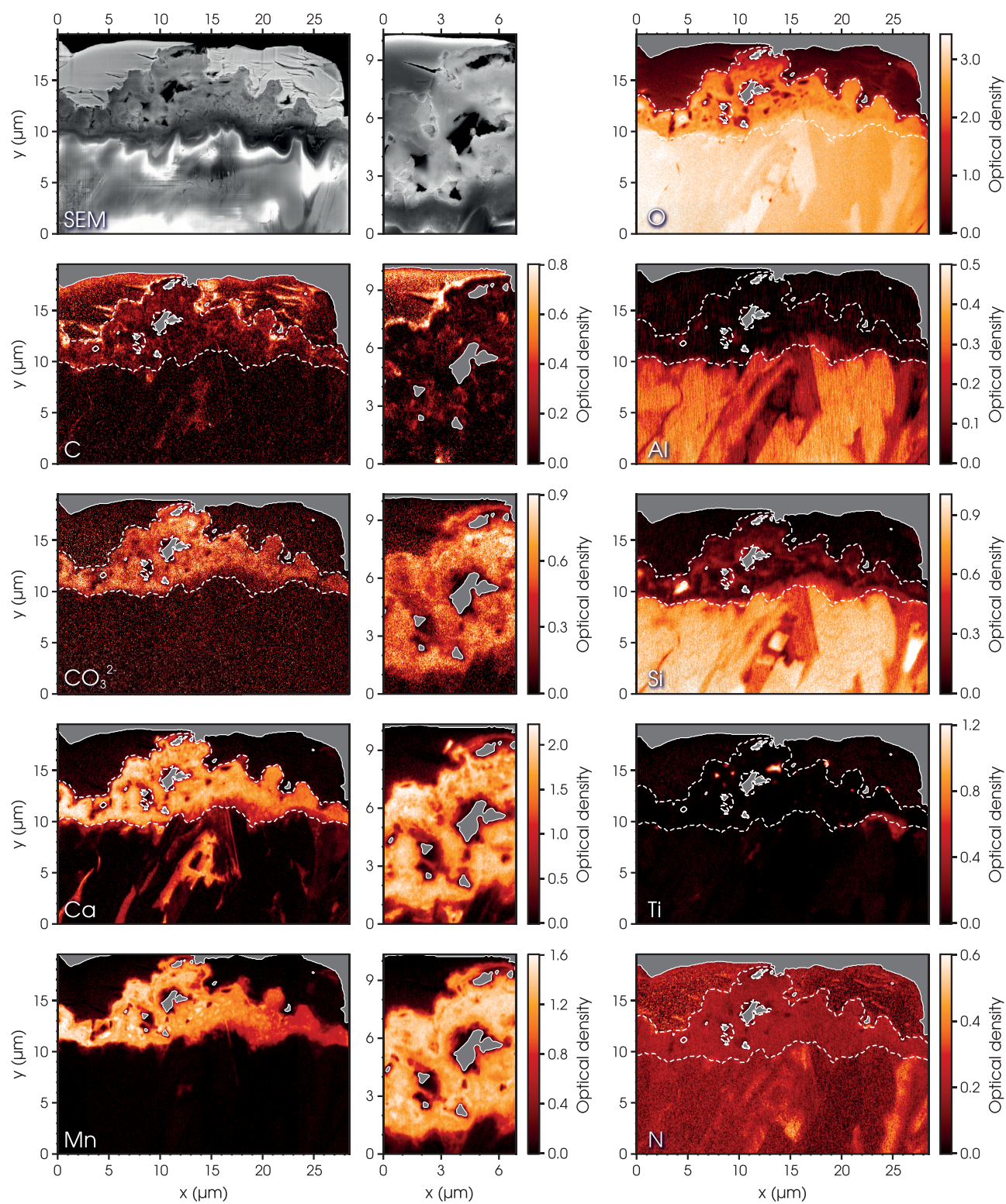
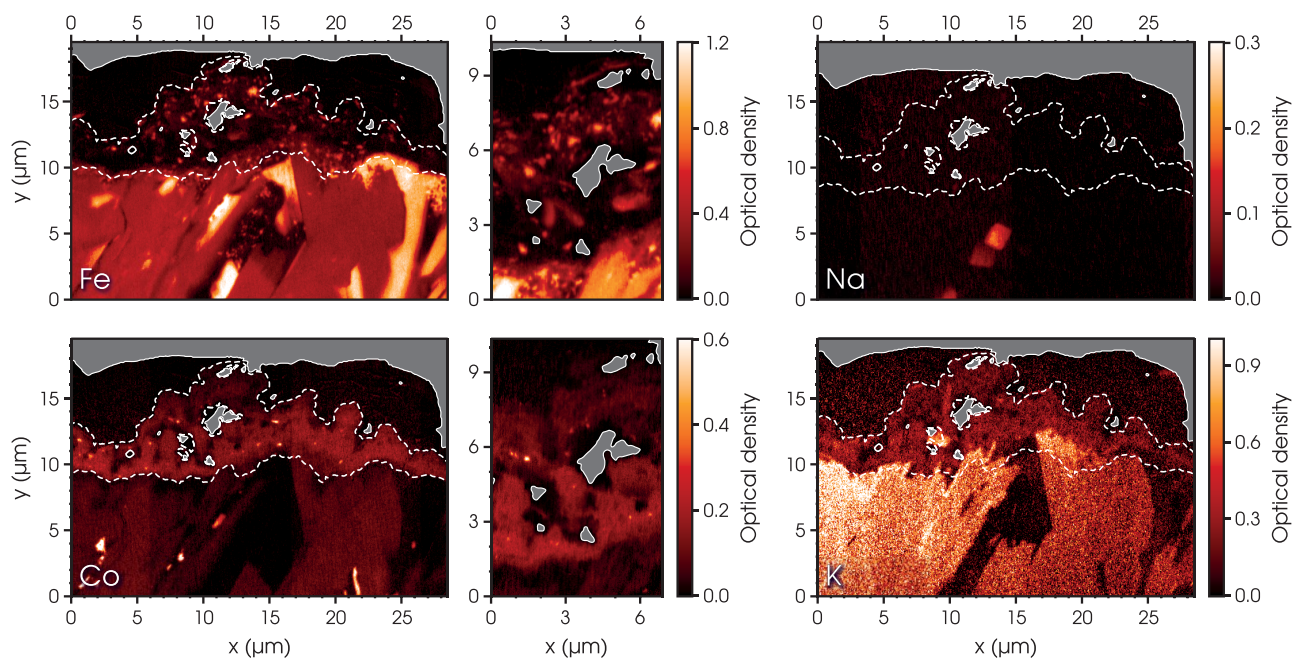


Figure 3. continued



**Figure 3.** SEM and STXM overviews of the urban varnish sample SC. The STXM maps represent the distribution of 12 different elements as well as the functional group  $\text{CO}_3^{2-}$ . The STXM maps in the left and right columns cover most of the varnish coating within the FIB slice (at 50 nm pixel size). The STXM maps in the central column represent rescans of a subregion in the maps in the left column at higher resolution (at 30 nm pixel size). The white dashed lines have been defined relative to the Mn-enriched region, which is indicative for the spatial extent of the varnish coating. Thus, the white lines help to visually separate the protective Pt coating from the varnish coating and from the underlying sandstone. The energy pairs at which the images for the STXM maps were recorded are shown as vertical lines in Figure 2. The almost homogeneously distributed levels of N in the varnish region correspond to the “bump” in Figure 2 and can therefore be seen as an artifact.

Each image contained  $40 \times 40$  diffraction patterns that provided a field of view of  $3.2 \times 3.2 \mu\text{m}^2$ . For the detection of diffraction patterns in transmission mode, a fast in-vacuum CCD camera, developed by PNSensor (Munich, Germany),<sup>68</sup> was utilized. The camera operates with a high frame rate of 450 Hz, having  $264 \times 264$  pixels and a pixel size of  $48 \mu\text{m}$ . It was placed downstream of the sample at a distance of 8 cm. A detailed description of the complete setup is given by Bykova.<sup>14</sup>

Diffraction images at each scanning point were dynamically stacked for 100 ms to provide sufficient photon count rates at high diffraction orders in reciprocal space. The dark field, with a closed beam shutter, was recorded prior to each ptychographic scan and subsequently subtracted from the diffraction patterns. Ptychographic reconstructions of phase and amplitude components were performed using the SHARP ptychography package developed for the ALS.<sup>69</sup> The iterative process consisted of 200 iterations of the Relaxed Averaged Alternating Reflections (RAAR) algorithm, including illumination and background retrieval. Streaking, due to the lack of a global shutter and a fixed-pattern noise were corrected during the reconstructions and remnants were manually removed in postprocessing via 2D FFT-filtering. This procedure was applied to all ptychographic reconstructions through the use of ImageJ v1.52a.<sup>66</sup> A custom macro was written to consistently apply a FFT-filter mask to all reconstructions.

## RESULTS AND DISCUSSION

**STXM-NEXAFS in Rock Varnish Analysis.** For all three varnish samples discussed in this work, X-ray absorption spectra, spanning multiple element absorption edges, are shown in Figure 2. The spectra show the characteristic

absorption peaks by the varnish-relevant 2p and 3d elements in the experimentally accessible X-ray energy range. Expectedly, the most pronounced X-ray absorption was found for O and Mn. Beyond the edge height reflecting the total element abundance, every absorption edge is characterized by NEXAFS features, providing spectral information on the chemical environments and valence states of the absorbing atoms.

The *K*-edges of the elements C, N, and O each represent an overlay of a single steplike absorption edge and NEXAFS features, consisting of sharp resonance peaks that correspond to certain functional groups.<sup>6</sup> At the C *K*-edge, all samples in Figure 2 show defined spectral peaks for  $\pi$ -bonds (285.0 eV) as well as carboxylic acid groups (COOH, at 288.4 eV). Noticeable is the pronounced carbonate peak ( $\text{CO}_3^{2-}$ , at 290.3 eV) in the SC varnish, in contrast to the samples CA WS18 and CA14 JC8, where much weaker  $\text{CO}_3^{2-}$  signals were found. At the N *K*-edge, no clear spectral features beyond the “bump”, which appears to be a spectral artifact, were observed. At the O *K*-edge, transitions from the Mn oxy-hydroxide O 1s-states to unoccupied O 2p-states that are hybridized with Mn 3d-states occur between 528 and 535 eV in the varnish spectrum and are absent in the sandstone spectrum (see sample SC in Figure 2). Since these electrons transition to the metal 3d-states, they are sensitive to the Mn valence states.<sup>70</sup> The *L*<sub>3,2</sub>-edges of the elements K, Ca, Mn, Fe, and Co consist of doublets comprising the *L*<sub>3</sub> and *L*<sub>2</sub> edges, which are separated due to spin–orbit coupling. Both edges, *L*<sub>3</sub> and *L*<sub>2</sub>, consist of multiplets of further overlapping peaks, reflecting the chemical and electronic character of the metal 3d-states.<sup>8,70</sup> Accordingly, the *L*<sub>3,2</sub> signatures contain information on metal valence, which is particularly relevant for Mn and Fe in the context of the varnish analysis.

Based on the X-ray absorption spectra in Figure 2, STXM maps were recorded that reflect the spatial distribution of selected elements and/or functional groups within the varnish coating. In Figure 3, we present a comprehensive set of STXM maps for the urban varnish sample SC. The maps characterize the typically accessible spatial resolution of STXM in geological samples in comparison to the subsequently presented X-ray ptychography results. The smallest resolved features (e.g., in the Ca map) have a full width at half-maximum (fwhm) of about 100 nm. Note that the maps were recorded after adjustment of the beamline and microscope settings and, thus, represent experimentally optimized conditions. The maps provide novel insights into the composition and microstructure of the SC varnish and, thus, complement the observations by Vicenzi et al.<sup>29</sup> and Sharps et al.<sup>52</sup> as discussed in the subsequent sections.

X-ray microspectroscopy on FIB slices provides a cross-sectional analysis of the varnish microstructure and composition, and thus allows us to precisely discriminate between the varnish coating and the underlying stone. Here, the Mn map represents the primary marker for the spatial extent of the varnish coating by means of the strong Mn enrichment in the varnish relative to the sandstone. The thickness of the varnish within the field of view of Figure 3 ranges from ~1 to ~8  $\mu\text{m}$ , which is much thicker than the fields of view analyzed by Sharps et al.,<sup>52</sup> ranging from ~150 to ~900 nm. In terms of the strong Mn enrichment in the varnish, our observations agree well with previous findings.<sup>29,52</sup> In terms of sandstone composition, high abundances of the oxides  $\text{SiO}_2$ ,  $\text{Al}_2\text{O}_3$ ,  $\text{Fe}_2\text{O}_3$ ,  $\text{Na}_2\text{O}$ , and  $\text{K}_2\text{O}$  have been reported,<sup>29,52</sup> which is in agreement with the high levels of Al, Si, Fe, and K in the stone in Figure 3. The only exception is Na, which shows a rather low abundance in Figure 3.

A particular strength of STXM-NEXAFS is the potential to characterize carbonaceous matter in terms of its distribution and overall composition. For the varnish analysis, this is particularly relevant as it allows a search for “microbial entombment in the Mn oxide”.<sup>29</sup> However, the maps of the potential biomarkers C and N in Figure 3 do not provide any indications for microbial structures. In fact, most of the C in the varnish appears to be bound in  $\text{CO}_3^{2-}$ .

Relative to the strong varnish-to-stone enrichment of Mn, Vicenzi et al.<sup>29</sup> reported an enrichment of further elements as follows:  $\text{Mn} \gg \text{Pb} > \text{Ca}, \text{Zn}, \text{Cu}, \text{Ni}$  and Sharps et al.<sup>52</sup> underline, in a follow-up study, that Mn, O, and Ca are the most abundant elements in the coating. This is in good agreement with our observations in Figures 2 and 3 showing a varnish-to-stone enrichment in Mn, Ca, C (specifically  $\text{CO}_3^{2-}$ ), and Co. Moreover, Figure 3 suggest lower levels of Al, Si, and Fe in the varnish.

Along the lines of these qualitative results, we conducted a quantitative correlation analysis of pixelwise optical density (OD) values (representing element/functional group abundances) of all maps in Figure 3 relative to Mn. Note that this correlation analysis was exclusively conducted for the varnish coating layer. Here, a positive linear correlation between Mn and a given element suggests that this element plays a constitutive role in the mineralogy of the Mn oxy-hydroxide, whereas a negative linear correlation or the absence of a clear relationship suggests that the given element is not mineralogically associated with the Mn oxy-hydroxide matrix. We found rather clear positive and linear correlations between Mn and

the following elements/functional groups (reported with the Pearson correlation coefficient,  $r$ ):

Ca ( $r = 0.82$ ),  $\text{CO}_3^{2-}$  ( $r = 0.51$ ), and Co ( $r = 0.33$ )

We further found negative, though strongly scattering, linear correlations between Mn and the following elements:

Si ( $r = -0.30$ ), Al ( $r = -0.28$ ), and Fe ( $r = -0.26$ )

No clear relationships were observed between Mn and C (without  $\text{CO}_3^{2-}$ ), K, N, Na, as well as Ti.

Further indications concerning the mineralogy of the Mn oxy-hydroxide matrix can be obtained from element ratios based on the multielement X-ray absorption spectra.<sup>5,71</sup> From the varnish spectrum in Figure 2 we obtained  $\text{O}/\text{Mn} = 2.5 \pm 0.1$ ,  $\text{Mn}/\text{Fe} = 20 \pm 3$ ,  $\text{Mn}/\text{Ca} = 17 \pm 3$ , and  $\text{Mn}/\text{C} = 4 \pm 3$ , which result in a stoichiometry of  $\text{C}_{0.5}\text{Ca}_{0.1}\text{Mn}_2\text{O}_5$  for the major elements with positive  $r$ . The corresponding data and calculations have been provided as supplementary data.<sup>72</sup> These results agree well with Vicenzi et al.<sup>29</sup> reporting  $\text{O}/\text{Mn} = 3.5$  and  $\text{Mn}/\text{Fe} = 20$  and do not contradict Sharps et al.,<sup>52</sup> who suggested that the layered phyllosilicate birnessite with an estimated stoichiometry of  $\text{Ca}_{0.3}\text{Mn}_2\text{O}_{4.4}$  constitutes the coating. Since we could show that  $\text{CO}_3^{2-}$  is enriched in the matrix, it is likely that much of the Ca present in the sample is bound as  $\text{CaCO}_3$  and unavailable for birnessite formation. However, our data neither support nor oppose an additional presence of birnessite in the varnish. Regardless of its exact composition, all these results agree that Ca acts as a major cation in the Mn oxy-hydroxide matrix and Na and K play a negligible role.

Vicenzi et al.<sup>29</sup> further reported “no discernible vertically definable substructure as opposed to microstratified varnish”. In Figure 3, the maps of those elements that are regarded as constitutive for the Mn oxy-hydroxides (i.e., Mn, O, Ca, Co) confirm this observation as they show a comparatively homogeneous appearance of the Mn matrix without any detectable stratification. In contrast, clear granular structures embedded into the Mn matrix were found for Fe and Ti. In the case of Fe, the observed grains could be explained either by embedded dust grains from atmospheric deposition or by Fe oxy-hydroxides, which could have coprecipitated independently of Mn oxyhydroxides in the course of the varnish formation.<sup>73</sup>

**X-ray Ptychography in Rock Varnish Analysis.** X-ray ptychography substantially improves the spatial resolution of “classical” STXM-NEXAFS analysis and preserves its analytical advantages, which are the high sensitivity to spectral features, and thus chemical contrasts, as well as the comparatively low degree of beam damage.<sup>8,10</sup> In comparison, SEM and TEM analyses provide an even higher spatial resolution, however, at the expense of lower chemical sensitivity and significantly higher levels of beam damage.<sup>74</sup> The following sections illustrate the analytical scope of X-ray ptychography in a geoscientific context by means of its first application to rock varnish analysis. For this, we focus on the amplitude data, which provide information on the absorption contrasts in the sample. The phase reconstructions have been retrieved as well and are provided as supplementary data,<sup>72</sup> however, due to a lack of suitable reference compounds and the largely unknown sample composition, interpretation of the refractive properties would be highly speculative and are therefore not addressed within the scope of this study.

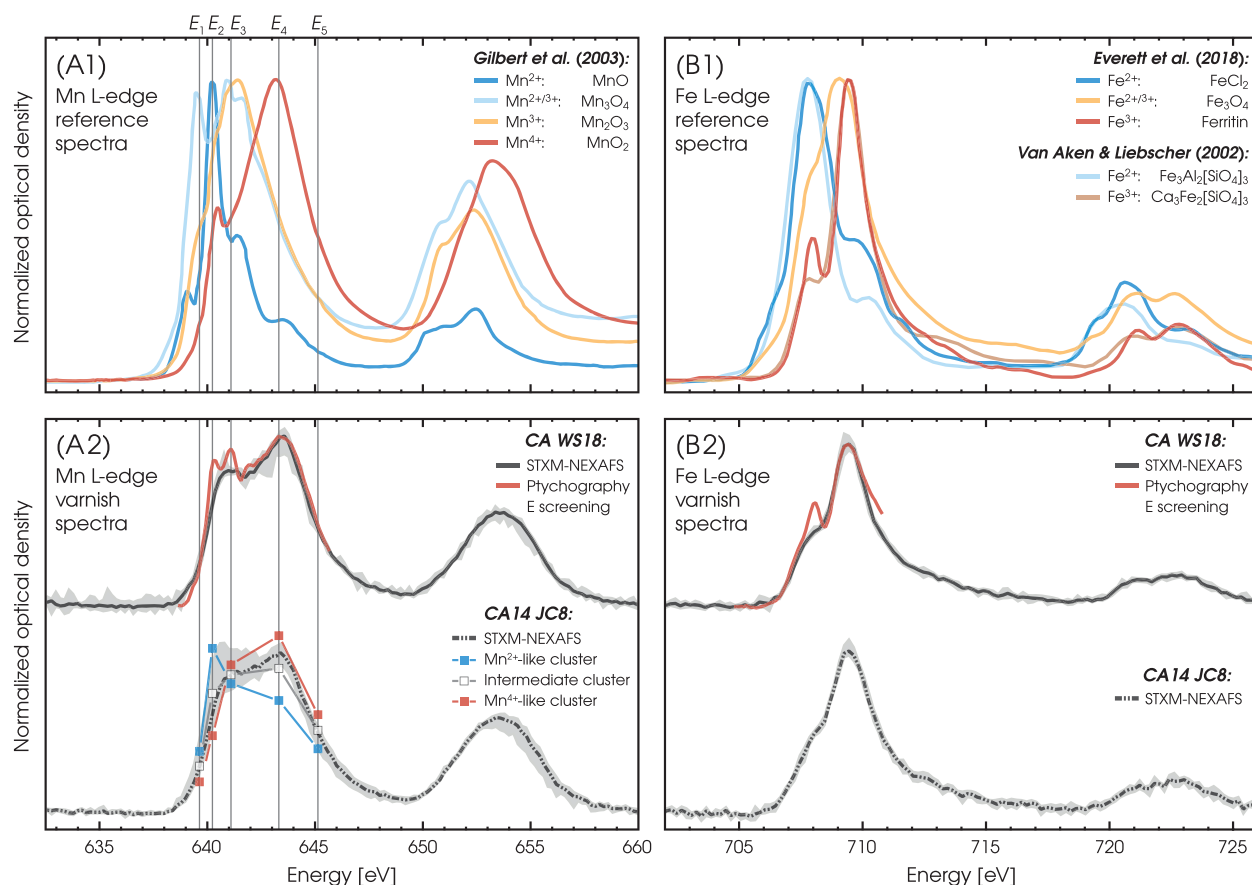


**Figure 4.** Manganese (A1) and iron (B1)  $L_{3,2}$ -edge spectra of reference compounds from literature sources<sup>1,74,77</sup> as well as Mn and Fe  $L_{3,2}$ -edge spectra of varnish samples CA WS18 (A2) and CA14 JC8 (B2) acquired by STXM-NEXAFS analysis. The reference spectra show spectral variability related to Mn and Fe oxidation states. Overall, the varnish spectra of CA WS18 (solid black) and CA14 JC8 (dashed black) are shown with gray shading emphasizing the spectral variability within the integrated varnish regions. Gray shading was obtained from envelope curves after partitioning the spectral signatures by means of a  $k$ -means cluster analysis ( $k = 7$ ). Mn (A2) and Fe (B2) spectra of sample CA WS18 were obtained roughly in regions C1 and D1 in Figure 5. Overall, STXM spectra correspond well with energy ( $E$ ) screening point-scan spectra (red solid lines) collected prior to ptychography imaging to correct potential energy offsets and to identify appropriate contrasting spectral features for ptychography scans. Energies for ptychographic imaging are shown as vertical lines at energies ( $E_1$ – $E_5$ ) for CA WS18 and CA14 JC8. Square data points in spectrum of CA14 JC8 (A2) were obtained from  $k$ -means cluster analysis ( $k = 3$ ) on the ptychography image stack (images at  $E_1$ – $E_5$ ). The resulting five-point cluster spectra were area normalized and vertically stretched such that the intermediate cluster spectrum (white boxes) matches well with the dash double-dotted spectrum.

The chemical reactions of the elements Mn and Fe are regarded as key factors in the uniquely slow growth of the varnish layers.<sup>73</sup> Thus, knowledge on their valence states is of particular importance for a deeper understanding of the Mn and Fe oxy–hydroxide mineralogy as well as its precipitation mechanism. However, nanoscale measurements of the Mn and Fe oxidation states in rock varnish coatings as well as related geological samples have remained sparse.<sup>75,76</sup> Figure 4 shows the  $L_{3,2}$ -edges of selected reference compounds along with their diverse spectral signatures that allow discriminating between geologically relevant Mn and Fe oxidation states (i.e.,  $Mn^{2+}$ ,  $Mn^{3+}$ ,  $Mn^{4+}$  and  $Fe^{2+}$ ,  $Fe^{3+}$ ). Moreover, Figure 4 zooms in on the  $L_{3,2}$ -edges of the arid desert rock varnish samples CA WS18 and CA14 JC8, as introduced in Figure 2, which both belong to type I varnish according to Macholdt et al.<sup>48</sup>

The comparison of the reference vs varnish spectra (Figure 4A1,B1 vs A2,B2) highlights the following aspects: Overall, both show a good agreement in terms of their spectral signatures. In particular, comparatively sharp features/peaks occur in the varnish spectra, which find their counterparts in the reference spectra (e.g., Mn peaks at 640.2 and 641.1 eV; Fe

peak at 707.9 eV). These features/peaks are more pronounced for the energy screening point scan spectra<sup>7</sup> (red lines in Figure 4A2,B2) compared to the STXM-NEXAFS spectra from scans over larger sample areas (black lines in Figure 4A2,B2). Iron in both samples predominantly occurs as  $Fe^{3+}$  as evident from the defined spectral shape of the Fe spectra (see gray shadings in Figure 4B2). This is not surprising since  $Fe^{3+}$  is the more stable oxidation state in Fe oxides and hydroxides under aerobic conditions. In contrast, the Mn spectra show a higher diversity (see rather broad gray shadings in Figure 4A2), suggesting that a mixture of the oxidation state  $Mn^{3+}$  and  $Mn^{4+}$ , probably also with some  $Mn^{2+}$ , occurs in the samples. The diversity of Mn oxidation states is higher for CA14 JC8 than for CA WS18.

Recently, we reported in Macholdt et al.<sup>8</sup> that the FIB preparation process of ultrathin slices as utilized here alters the Mn oxidation states through a near-surface reduction of  $Mn^{4+}$  to  $Mn^{2+}$ . This implies that the Mn spectra in Figure 4A2 show a more reduced valence state distribution than the supposed original Mn oxidation in the varnish. Evidently, this beam damage effect fundamentally precludes drawing overall

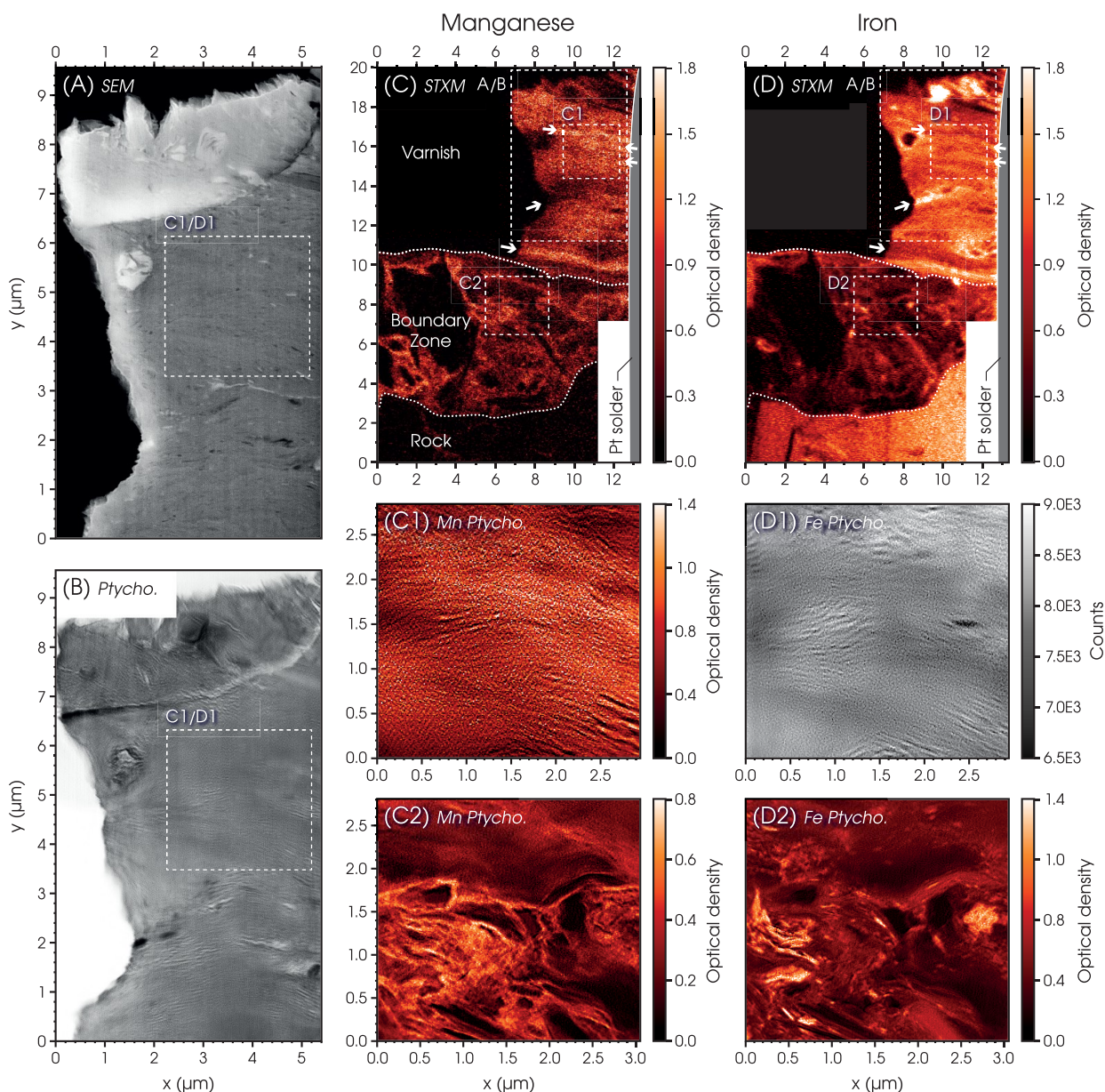


**Figure 5.** Micrographs of sample CA WS18 reveal a complex morphology. (A) (SEM micrograph, detector: SE2) and (B) (composite of three individual ptychographic reconstructions at 797.7 eV) show the varnish-dominated subregion emphasized in panels C and D. The distribution of chemical elements within the varnish-dominated surface layers down to the rock and clay-mineral-rich underground material is shown via optical density maps for manganese in subfigures C (635.0/642.0 eV), C1 (639.7/643.4 eV), and C2 (639.7/643.3 eV) and for iron in subfigures D (704/709.5 eV) and D2 (708.5/710.2 eV), respectively. Panel D1 displays the single-energy X-ray absorption micrograph at 710.3 eV only. While panels C and D reveal an alternating pattern of iron- and manganese-rich structures in the near-surface varnish-dominated region with a width of a few hundred nanometers, a finer underlying sheet structure is visible in C1 and D1. In the boundary zone, nanometer-scale iron containing granules are contrasting the Mn and Fe-rich varnish matrix as seen in C2 and D2. Color scales in OD, gray scale in counts. All axes in  $\mu\text{m}$ .

conclusions on the average and authentic Mn oxidation state in the varnish. On the nanoscale, however, we can conjecture that the *distribution and patterns* of contrasting Mn valence states remained unaffected since the artificial reduction acts homogeneously on the entire surfaces of the FIB slices, which is a plausible assumption. Throughout the subsequent sections, our results are discussed carefully with consideration of the artificial beam-related Mn reduction outlined here.

Figure 5 presents a combination of SEM, STXM, and ptychography micrographs from sample CA WS18. The Mn and Fe STXM overview maps in Figure 5C,D show a remarkable 3-fold division along the depth profile, comprising

(i) an upper stratified varnish layer, (ii) a varnish/rock boundary zone of more granular appearance, with clay minerals embedded into the varnish matrix, and (iii) the underlying rock (see dotted lines as separators in Figure 5C,D). Ptychography was applied to selected subregions to resolve nanoscale structures within the stratified varnish layer as well as within the varnish/rock boundary zone (Figure 5C1,C2 vs D1,D2). The corresponding ptychography maps and images were recorded with a pixel size of  $\sim 12.2$  nm/px and  $\sim 11.0$  nm/px for Mn and Fe, respectively.

The type I varnish in Figure 5 contrasts with the urban varnish from Figure 3. A characteristic feature of type I varnish

is the alternation of Mn- and Fe-rich layers inside the matrix, visible in the STXM element distribution maps shown in Figure 5 and discussed in Garvie et al.<sup>44</sup> and Macholdt et al.<sup>49</sup> In panels C and D in Figure 5 the alternating pattern of the Mn/Fe microlaminations is emphasized by arrows pointing in the propagation direction of some individual layers.

The morphological differences between the varnish region (Figure 5C1/D1) and the boundary zone (Figure 5C2/D2) become obvious from the ptychographic reconstructions. The boundary zone consists of a fabric of clay minerals cemented by a Mn- and Fe-rich matrix.<sup>49</sup> In addition to this gap-filling material interconnecting the clay mineral grains, nanometer-scale iron-containing granules (which we had not previously seen with conventional STXM) are abundant in the matrix (Figure 5D2), whereas the varnish region itself is relatively free of clay minerals and shows no Fe-rich granules. Similar granules had been observed by Vicenzi et al.<sup>29</sup> by SEM X-ray elemental mapping in the void-filling material of the SC varnish.

This finding appears plausible with reference to the aqueous atmospheric deposition model proposed by Thiagarajan and Lee.<sup>19</sup> Dust grains that deposit on a previously smoothed surface, i.e., when pores and cavities within the rock surface have already been sealed by previous growth of varnish or silica glaze, are easily flushed away by water or blown off the surface by wind. However, if the surface is still unprocessed and porous, dust particles get trapped and will be embedded interstitially. One possible explanation for the Fe-rich grains inside the boundary zone is that these are residual airborne dust particles cemented in the varnish matrix. Contrastingly, larger Fe-rich granules were found in the urban varnish discussed above (Figure 3), which reach up to the surface of the varnish. As for the slower growing type I varnish, physical removal of dust particles is possible over a much longer period of time, so that growth rates could have a large influence on the amount of incorporated particles. However, it is also possible that the Fe-rich grains are not associated with dust deposition, but formed later as precipitates inside the varnish matrix. Besides the mentioned stratification (compare parts C and C of Figure 5), the only substructure visible in the varnish dominated region is a ripple pattern that looks like Moiré fringes at first glance. For the most part, this pattern cannot be attributed to ringing artifacts produced by the reconstruction algorithm, whose spacing is in the same size range, but must be a real structure, for the following reasons: (i) It appears in all reconstructions at different energies at the same spots (compare Figure 5B and C1 and D1). (ii) The pattern is roughly oriented in parallel to the rock surface and follows the overall direction of the stratification. (iii) Special care was taken during the alignment of the reconstructions used in Figure 5C1 to avoid an accidental enhancement of the ripples. We interpret the ripples as up to a few tens of nanometers-sized lamellae of varying chemical composition (consistent with EFTEM results shown by Garvie et al.<sup>44</sup>). These lamellae overlap with and interpenetrate each other, resembling a stack of folded and rolled-up sheets of paper. Because the FIB slice of sample CA WS18 is rather thick (420 nm) compared to the spacing of the lamellae, the visibility of the ripples can either be preserved in the case of perfect orientation of the layers along the line of sight, or fully disappear, by means of constructive and destructive interference. Most likely the latter case is coming into effect here and obscures the underlying structures.

A second sample, CA14 JC8, was also selected for ptychography. Unlike sample CA WS18, it could be investigated in a highly thinned region with only about a quarter of the other sample's thickness. In Figure 6A the SEM

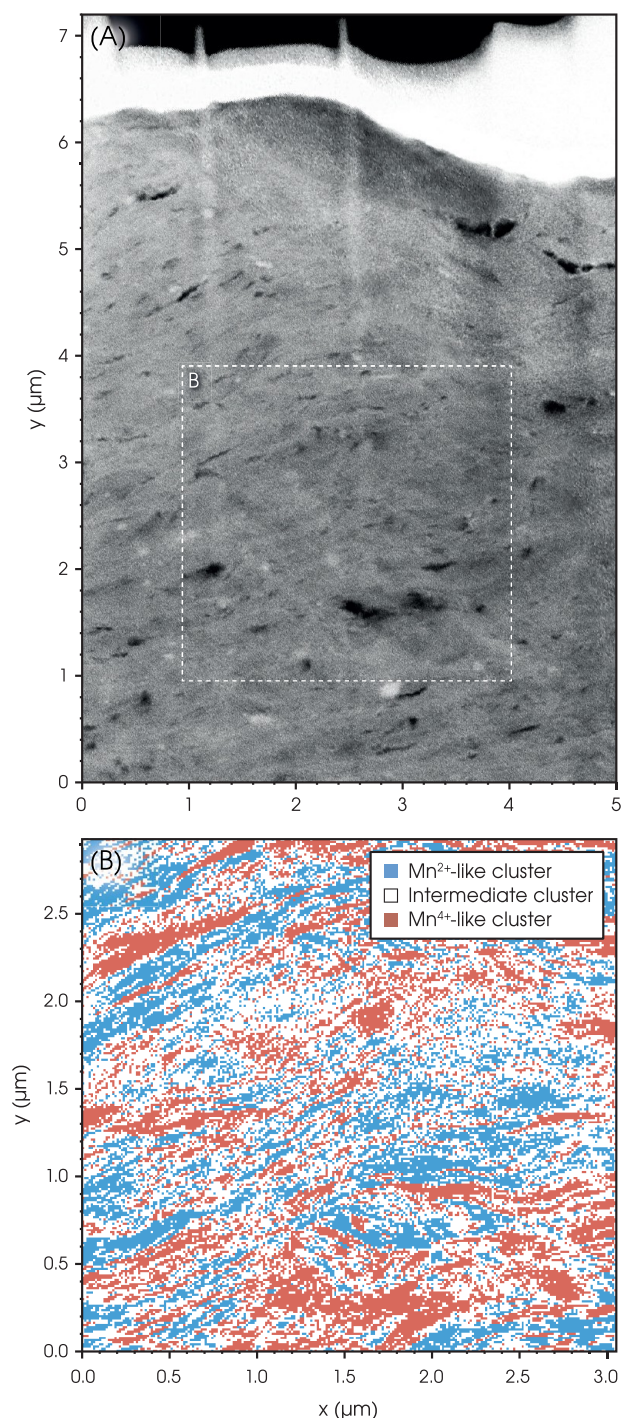


**Figure 6.** (A) SEM micrograph of the upper part of sample CA14 JC8. The region of interest, in which ptychography scans at the Mn *L*-edge were conducted, is denoted as B and located in a thin region of the FIB slice (~100–200 nm). (B) Result of the three-cluster ( $k = 3$ )  $k$ -means cluster analysis on a five-energy-point ptychography stack with 12.2 nm by 12.2 nm pixel size show not only laminar Mn-enriched structures but reveal an alternating pattern of different valence states. The corresponding cluster spectra are shown in Figure 4.

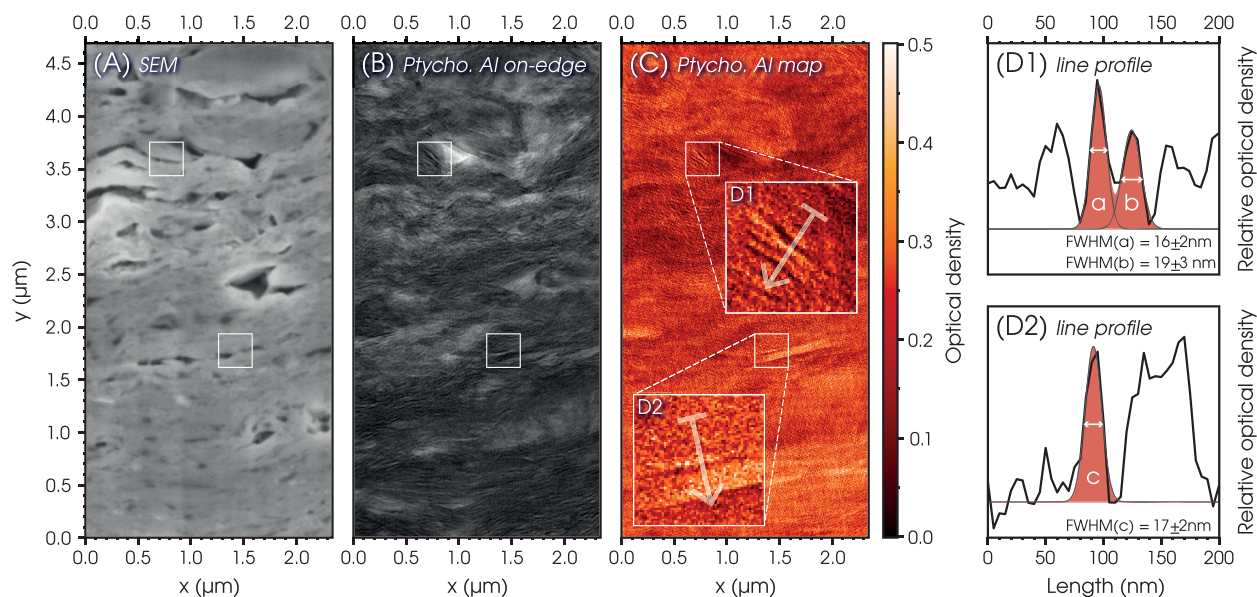


**Figure 7.** Different views of the same region on sample CA14 JC8,  $\sim 20 \mu\text{m}$  below Figure 6B: (A) SEM micrograph; (B) ptychographic reconstruction at the Al edge with 5 nm/px resolution at  $\sim 1569 \text{ eV}$  and (C) corresponding ptychographic optical density map ( $\sim 1565 \text{ eV}$  /  $\sim 1569 \text{ eV}$ ). In panels D1 and D2 line profiles (200 nm length and 60 nm width (12 px average), perpendicular to Al-rich structures) resolve details with 16–19 nm fwhm.

micrograph illustrates the physical distance to the sample surface, which is covered by the residues of the Pt stripe. Figure 6B represents the results of the ptychographic analysis in the form of a  $k$ -means cluster analysis (CA) with three clusters ( $k = 3$ ) and five energy points ( $E_1$ – $E_5$ ) instead of a simple OD map. We chose this representation here because it is more robust against fringing artifacts (doubled edges) and statistically more significant (5 energy points for CA vs 2 energy points for an OD map). The CA clearly differentiates the sample by the spectral signatures representing a  $\text{Mn}^{2+}$ -like, a  $\text{Mn}^{4+}$ -like, and an intermediate state (mixed-valence or  $\text{Mn}^{3+}$ ). A stratified pattern and an alternation of valence states is clearly visible. Because of the artifactual origin of an unknown amount of the  $\text{Mn}^{2+}$  in the sample, the ptychographic data allow no quantitative interpretation at this point. However, we can show that X-ray ptychography has the ability to resolve such structures on the nanoscale.

Another noticeable difference between the SEM micrograph and the result of the ptychographic cluster analysis results in Figure 6 is the very weak visibility of the laminar structures in the SEM image. This can be attributed to (i) the surface-sensitive view of the SEM compared to the penetrating nature of the X-ray image and/or (ii) the sample preparation method. During FIB slicing, the outermost few nanometers of a sample, which are seen by SEM, are affected by amorphization, as detailed in Macholdt et al.<sup>8</sup>

In ptychography, the achievable spatial resolution depends on several factors, e.g., the detector's pixel size and area, the numerical aperture of the zone plate, the thermal/mechanical stability of the microscope, and inherent sample properties, e.g., the scattering contrast at the selected X-ray energies as detailed in Bykova.<sup>14</sup> In the present case, where a porous and thus highly structured geological sample with a suitable sample thickness of a few hundred nanometers exhibits satisfying absorption and refraction contrasts in the soft X-ray regime, the achievable resolution scales predominantly with the X-ray energy, because at a higher energy, the CCD detector captures

more of the photons in the far-field diffraction orders, which miss the detector at lower energies and thus lead to a poorer reconstruction result.

This effect is emphasized in Figure 7, which shows ptychographic imaging at the Al K-edge with a pixel size of  $5 \times 5 \text{ nm}^2$ . The smallest Al-rich structures detected in Figure 7C were in the size range of 16–19 nm fwhm (compare Figure 7D1,D2). To quantify the resolution achieved, a Fourier ring correlation (FRC) analysis<sup>78</sup> has been performed using the BIOP/ijp-frc plugin<sup>79</sup> in Fiji/ImageJ 1.52n (Java 8) on the amplitude and phase reconstructions at  $\sim 1565$  and  $\sim 1569 \text{ eV}$ . Half-bit thresholding<sup>78</sup> yielded FIRE (Fourier Image REsolution) numbers<sup>80</sup> of down to 14 nm (amplitude) and 12.5 nm (phase), respectively, in selected subregions of the total image area. This agrees well with the measured feature widths. Ideally, FRC would have been performed on two images with identical recording parameters, only distinguishable by the noise pattern. Such data were not available. While phase reconstructions at the two different energies were very similar to each other, the amplitude reconstructions on the other hand contained differences in absorption properties as seen from the Al map in Figure 7C, which lead to a worse correlation and therefore a lower FIRE number. The corresponding results, raw and processed phase and amplitude reconstructions have been deposited in Edmond, the Max Planck Society's open-access data repository<sup>72</sup>

## CONCLUSIONS

This study presents a comparison between STXM-NEXAFS and X-ray ptychography as applied to the analysis of rock varnish samples. The analytical strength of STXM with ptychography is defined by its unique combination of nanoscale imaging, high spectroscopic and thus chemical sensitivity, and comparatively low levels of beam damage. NEXAFS spectroscopy was used to illustrate the chemical imaging capabilities of STXM-NEXAFS analysis for rock varnish. The X-ray absorption spectra for Mn and Fe reveal a

predominant presence of Fe<sup>3+</sup> as well as a mixture of the Mn valence states Mn<sup>4+</sup>, Mn<sup>3+</sup>, and Mn<sup>2+</sup> in the varnish. Generally, the spectral features observed are in good agreement with previously reported literature values on reference compounds.<sup>1,74,77</sup> Chemical/elemental maps provide an overview on the spatial distribution of various elements inside the rock and the varnish layer. A set of micrographs was used to identify those elements that are associated with the mineralogy of the Mn-rich matrix. Our findings agree well with the results provided by Vicenzi et al.<sup>29</sup> and Sharps et al.<sup>52</sup> on the SC varnish and complement previous findings by providing further quantitative insights.

X-ray ptychography was applied to two arid desert varnish samples. Ptychography increases the spatial resolution relative to STXM by up to 1 order of magnitude and thus allows resolving structural features and chemical contrasts that have remained invisible in previous STXM investigations. The rock varnish samples revealed clear structural and compositional differences between regions of stratified varnish growth vs a varnish/rock boundary zone with more granular appearance, which is presumably due to embedded mineral dust grains. At the highest spatial and spectroscopic sensitivities that ptychography can provide, remarkable nanoscale stratifications with layers of alternating Mn valence states were observed. Although beam damage effects cannot be neglected here, the nanostratification appears to be an authentic feature of the arid varnish coating.<sup>49</sup> A further investigation of the nanostratification may provide novel insights into the growth of the varnish layer, since the thickness of these layers corresponds with the estimated annual growth rates of arid desert varnish.<sup>73</sup> The highest spatial resolution in the course of the entire study was obtained at the Al absorption edge, where structures of about 16 nm fwhm were resolved.

## AUTHOR INFORMATION

### Corresponding Authors

**Jan-David Förster** – *Multiphase Chemistry Department, Max Planck Institute (MPI) for Chemistry, Mainz 55128, Germany; Biogeochemistry Department, Max Planck Institute for Chemistry, Mainz 55128, Germany; [orcid.org/0000-0001-6758-8396](https://orcid.org/0000-0001-6758-8396); Email: [jd.forster@mpic.de](mailto:jd.forster@mpic.de)*

**Christopher Pöhlker** – *Multiphase Chemistry Department, Max Planck Institute (MPI) for Chemistry, Mainz 55128, Germany; Biogeochemistry Department, Max Planck Institute for Chemistry, Mainz 55128, Germany; [orcid.org/0000-0001-6958-425X](https://orcid.org/0000-0001-6958-425X); Email: [c.pohlker@mpic.de](mailto:c.pohlker@mpic.de)*

### Authors

**Iuliia Bykova** – *Modern Magnetic Systems Department, MPI for Intelligent Systems, Stuttgart 70569, Germany; Present Address: Laboratory for Micro and Nanotechnology, Photon Science Division, Paul Scherrer Institut, Villigen, Switzerland*

**Dorothea S. Macholdt** – *Biogeochemistry Department and Climate Geochemistry Department, Max Planck Institute for Chemistry, Mainz 55128, Germany*

**Klaus Peter Jochum** – *Biogeochemistry Department and Climate Geochemistry Department, Max Planck Institute for Chemistry, Mainz 55128, Germany*

**Michael Kappl** – *Physics at Interfaces Department, Max Planck Institute for Polymer Research, Mainz 55128, Germany; [orcid.org/0000-0001-7335-1707](https://orcid.org/0000-0001-7335-1707)*

**A. L. David Kilcoyne** – *Advanced Light Source, Lawrence Berkeley National Laboratory, Berkeley 94720-8225, United States; [orcid.org/0000-0002-8805-8690](https://orcid.org/0000-0002-8805-8690)*

**Maren Müller** – *Physics at Interfaces Department, Max Planck Institute for Polymer Research, Mainz 55128, Germany*

**Antje Sorowka** – *Particle Chemistry Department, Max Planck Institute for Chemistry, Mainz 55128, Germany*

**Bettina Weber** – *Multiphase Chemistry Department, Max Planck Institute (MPI) for Chemistry, Mainz 55128, Germany; Present Address: Institute of Biology, Division of Plant Sciences, University of Graz, Austria.*

**Markus Weigand** – *Institute for Nanospectroscopy, Helmholtz-Zentrum Berlin für Materialien und Energie GmbH, Berlin 12489, Germany*

**Gisela Schütz** – *Modern Magnetic Systems Department, MPI for Intelligent Systems, Stuttgart 70569, Germany*

**Meinrat O. Andreae** – *Biogeochemistry Department, Max Planck Institute for Chemistry, Mainz 55128, Germany; Scripps Institution of Oceanography, University of California San Diego, La Jolla 92093, United States; Department of Geology and Geophysics, King Saud University, Riyadh 11362, Saudi Arabia*

Complete contact information is available at:

<https://pubs.acs.org/10.1021/acs.jpcc.1c03600>

### Author Contributions

STXM-NEXAFS analyses were performed by J.-D.F., D.S.M., C.P., M.O.A., and B.W., supported by A.L.D.K. and M.W. Ptychography measurements were carried out by J.-D.F. and I.B., supported by M.W. The FIB samples were prepared by M.M., supported by M.K. The SEM characterization was conducted by A.S. and J.-D.F. Data were processed and visualized by J.-D.F., I.B., and C.P. The manuscript was written by J.-D.F. and C.P., with contributions from I.B., D.S.M., and M.O.A. C.P. and M.O.A. conceptualized this study with contributions from G.S., M.W., and K.P.J. All authors contributed to the discussion of the results, reviewed the paper, and gave approval to the final version of the manuscript.

### Funding

Open access funded by Max Planck Society.

### Notes

The authors declare no competing financial interest.

## ACKNOWLEDGMENTS

This work was supported by the Max Planck Society, the Max Planck Graduate Center with the Johannes Gutenberg University Mainz (MPGC), and the King Saud University. This research used resources of the Advanced Light Source, which is a DOE Office of Science User Facility under Contract No. DE-AC02-05CH11231. We thank the Helmholtz-Zentrum Berlin for the allocation of the synchrotron radiation beam time at BESSY II. We kindly acknowledge Tanzhuo Liu for providing the arid desert varnish sample CA WS18 and Richard A. Livingston for providing urban varnish sample SC. Furthermore, we thank Michael Bechtel, Ingo Lieberwirth, Ulrich Pöschl, and Gerald Haug for their support and stimulating discussions.

## ADDITIONAL NOTE

<sup>†</sup>With “energy screening point scan spectra”—in short “ptychography E screening”—we refer to energy scans with

an illumination spot diameter of about 100  $\mu\text{m}$  at a fixed beam location on the sample. These scans were conducted prior to ptychography image stack scans in order to resolve the precise position of spectral features and to define the most appropriate energies for the ptychography images to achieve the best chemical contrast.

## REFERENCES

- (1) Van Aken, P. A.; Liebscher, B. Quantification of ferrous/ferric ratios in minerals: New evaluation schemes of Fe L23 electron energy-loss near-edge spectra. *Phys. Chem. Miner.* **2002**, *29*, 188–200.
- (2) Thieme, J.; Sedlmair, J.; Gleber, S.-C.; Prietzel, J.; Coates, J.; Eusterhues, K.; Abbt-Braun, G.; Salome, M. X-ray spectromicroscopy in soil and environmental sciences. *J. Synchrotron Radiat.* **2010**, *17*, 149–157.
- (3) Ault, A. P.; Axson, J. L. Atmospheric Aerosol Chemistry: Spectroscopic and Microscopic Advances. *Anal. Chem.* **2017**, *89*, 430–452.
- (4) Myneni, S. C. B. In *Applications of Synchrotron Radiation in Low-Temperature Geochemistry and Environmental Sciences*; Fenter, P. A., Rivers, M. L., Sturchio, N. C., Sutton, S. R., Eds.; Reviews in Mineralogy & Geochemistry; Mineralogical Society of America, 2002; Vol. 49; pp 485–579.
- (5) Moffet, R. C.; Tivanski, A. V.; Gilles, M. K. *Fundamentals and Applications in Aerosol Spectroscopy*; CRC Press, 2011.
- (6) Stöhr, J. *NEXAFS Spectroscopy*; Springer Series in Surface Sciences; Springer Berlin Heidelberg: Berlin, 1992; Vol. 25.
- (7) Ade, H.; Stoll, H. Near-edge X-ray absorption fine-structure microscopy of organic and magnetic materials. *Nat. Mater.* **2009**, *8*, 281–290.
- (8) Macholdt, D. S.; Förster, J.-D.; Müller, M.; Weber, B.; Kappl, M.; Kilcoyne, A. L. D.; Weigand, M.; Leitner, J.; Jochum, K. P.; Pöhlker, C.; et al. Artifacts from manganese reduction in rock samples prepared by focused ion beam (FIB) slicing for X-ray microspectroscopy. *Geosci. Instrum., Methods Data Syst.* **2019**, *8*, 97–111.
- (9) Shapiro, D. A.; Babin, S.; Celestre, R. S.; Chao, W.; Conley, R. P.; Denes, P.; Enders, B.; Enfedaque, P.; James, S.; Joseph, J. M.; et al. An ultrahigh-resolution soft x-ray microscope for quantitative analysis of chemically heterogeneous nanomaterials. *Science Advances* **2020**, *6*, No. eabc4904.
- (10) Shapiro, D. A.; Yu, Y. S.; Tyliczszak, T.; Cabana, J.; Celestre, R.; Chao, W. L.; Kaznatcheev, K.; Kilcoyne, A. L. D.; Maia, F.; Marchesini, S.; et al. Chemical composition mapping with nanometre resolution by soft X-ray microscopy. *Nat. Photonics* **2014**, *8*, 765–769.
- (11) Falcone, R.; Jacobsen, C.; Kirz, J.; Marchesini, S.; Shapiro, D.; Spence, J. New directions in X-ray microscopy. *Contemp. Phys.* **2011**, *52*, 293–318.
- (12) Hitchcock, A. P. Soft X-ray spectromicroscopy and ptychography. *J. Electron Spectrosc. Relat. Phenom.* **2015**, *200*, 49–63.
- (13) Farmand, M.; Celestre, R.; Denes, P.; Kilcoyne, A. L. D.; Marchesini, S.; Padmore, H.; Tyliczszak, T.; Warwick, T.; Shi, X.; Lee, J.; et al. Near-edge X-ray refraction fine structure microscopy. *Appl. Phys. Lett.* **2017**, *110*, 5.
- (14) Bykova, I. High-resolution X-ray ptychography for magnetic imaging. Ph.D. thesis, Universität Stuttgart, 2018; Publisher: Universität Stuttgart.
- (15) Donnelly, C.; Scagnoli, V.; Guizar-Sicairos, M.; Holler, M.; Wilhelm, F.; Guillou, F.; Rogalev, A.; Detlefs, C.; Menzel, A.; Raabe, J.; et al. High-resolution hard x-ray magnetic imaging with dichroic ptychography. *Phys. Rev. B: Condens. Matter Mater. Phys.* **2016**, *94*, 9.
- (16) Shi, X.; Fischer, P.; Neu, V.; Elefant, D.; Lee, J. C. T.; Shapiro, D. A.; Farmand, M.; Tyliczszak, T.; Shiu, H. W.; Marchesini, S.; et al. Soft x-ray ptychography studies of nanoscale magnetic and structural correlations in thin SmCo<sub>5</sub> films. *Appl. Phys. Lett.* **2016**, *108*, 094103.
- (17) Zhu, X. H.; Hitchcock, A. P.; Bazylinski, D. A.; Denes, P.; Joseph, J.; Lins, U.; Marchesini, S.; Shiu, H. W.; Tyliczszak, T.; Shapiro, D. A. Measuring spectroscopy and magnetism of extracted and intracellular magnetosomes using soft X-ray ptychography. *Proc. Natl. Acad. Sci. U. S. A.* **2016**, *113*, E8219–E8227.
- (18) Von Humboldt, A.; Bonpland, A. *Voyage aux Régions Équinoxiales du Nouveau Continent. II*; Schoell: Paris, 1819; pp299–277.
- (19) Thiagarajan, N.; Lee, C.-T. A. Trace-element evidence for the origin of desert varnish by direct aqueous atmospheric deposition. *Earth Planet. Sci. Lett.* **2004**, *224*, 131–141.
- (20) Hodge, V. F.; Farmer, D. E.; Diaz, T.; Orndorff, R. L. Prompt detection of alpha particles from Po-210: another clue to the origin of rock varnish? *J. Environ. Radioact.* **2005**, *78*, 331–342.
- (21) Dorn, R. I.; Krinsley, D. Spatial, temporal and geographic considerations of the problem of rock varnish diagenesis. *Geomorphology* **2011**, *130*, 91–99.
- (22) Liu, T.; Dorn, R. I. Understanding the Spatial Variability of Environmental Change in Drylands with Rock Varnish Microlaminations. *Annals of the Association of American Geographers* **1996**, *86*, 187–212.
- (23) DiGregorio, B. E. In *Instruments, Methods, and Missions for Astrobiology Iv*; Hoover, R. B., Levin, G. V., Paepe, R. R., Rozanov, A. Y., Eds.; Proceedings of the Society of Photo-Optical Instrumentation Engineers (Spie); Spie-Int Soc Optical Engineering: Bellingham, 2001; Vol. 4495; pp 120–130.
- (24) Perry, R. S.; Kolb, V. M. In *Instruments, Methods, and Missions for Astrobiology Vii*; Hoover, R. B., Rozanov, A. Y., Eds.; Proceedings of the Society of Photo-Optical Instrumentation Engineers (Spie); Spie-Int Soc Optical Engineering: Bellingham, 2004; Vol. 5163; pp 136–144.
- (25) Goldsmith, Y.; Stein, M.; Enzel, Y. From dust to varnish: Geochemical constraints on rock varnish formation in the Negev Desert, Israel. *Geochim. Cosmochim. Acta* **2014**, *126*, 97–111.
- (26) Kuhlman, K. R.; Venkat, P.; La Duc, M. T.; Kuhlman, G. M.; McKay, C. P. Evidence of a microbial community associated with rock varnish at Yungay, Atacama Desert, Chile. *Journal of Geophysical Research: Biogeosciences* **2008**, *113*, G04022.
- (27) Zerboni, A. Holocene rock varnish on the Messak plateau (Libyan Sahara): Chronology of weathering processes. *Geomorphology* **2008**, *102*, 640–651.
- (28) Krinsley, D. H.; Dorn, R. I.; DiGregorio, B. E.; Langworthy, K. A.; Ditto, J. Rock varnish in New York: An accelerated snapshot of accretionary processes. *Geomorphology* **2012**, *138*, 339–351.
- (29) Vicenzi, E. P.; Grissom, C. A.; Livingston, R. A.; Weldon-Yochim, Z. Rock varnish on architectural stone: microscopy and analysis of nanoscale manganese oxide deposits on the Smithsonian Castle, Washington, DC. *Heritage Sci.* **2016**, *4*, 14.
- (30) Lanza, N. L.; Clegg, S. M.; Wiens, R. C.; McInroy, R. E.; Newsom, H. E.; Deans, M. D. Examining natural rock varnish and weathering rinds with laser-induced breakdown spectroscopy for application to ChemCam on Mars. *Appl. Opt.* **2012**, *51*, B74–B82.
- (31) Perry, R. S.; Sephton, M. A. Desert varnish: an environmental recorder for Mars. *Astron. Geophys.* **2006**, *47*, 34–35.
- (32) Otter, L. M.; Macholdt, D. S.; Jochum, K. P.; Stoll, B.; Weis, U.; Weber, B.; Scholz, D.; Haug, G. H.; Al-Amri, A. M.; Andreae, M. O. Geochemical insights into the relationship of rock varnish and adjacent mineral dust fractions. *Chem. Geol.* **2020**, *551*, 119775.
- (33) Perry, R. S.; Lynne, B. Y.; Sephton, M. A.; Kolb, V. M.; Perry, C. C.; Staley, J. T. Baking black opal in the desert sun: The importance of silica in desert varnish. *Geology* **2006**, *34*, 537–540.
- (34) Schelble, R. T.; McDonald, G. D.; Hall, J. A.; Nealson, K. H. Community structure comparison using FAME analysis of desert varnish and soil, Mojave desert, California. *Geomicrobiol. J.* **2005**, *22*, 353–360.
- (35) Krumbein, W. E.; Jens, K. Biogenic rock varnishes of the Negev Desert (Israel) an ecological study of iron and manganese transformation by cyanobacteria and fungi. *Oecologia* **1981**, *50*, 25–38.
- (36) Dorn, R. I.; Oberlander, T. M. Microbial origin of desert varnish. *Science* **1981**, *213*, 1245–1247.
- (37) Northrup, D. E.; Snider, J. R.; Spilde, M. N.; Porter, M. L.; van de Kamp, J. L.; Boston, P. J.; Nyberg, A. M.; Bargar, J. R. Diversity of

rock varnish bacterial communities from Black Canyon, New Mexico. *Journal of Geophysical Research-Biogeosciences* **2010**, *115*, 19.

(38) Parchert, K. J.; Spilde, M. N.; Porras-Alfaro, A.; Nyberg, A. M.; Northup, D. E. Fungal Communities Associated with Rock Varnish in Black Canyon, New Mexico: Casual Inhabitants or Essential Partners? *Geomicrobiol. J.* **2012**, *29*, 752–766.

(39) Liu, T. Z.; Broecker, W. S. Millennial-scale varnish microlamination dating of late Pleistocene geomorphic features in the drylands of western USA. *Geomorphology* **2013**, *187*, 38–60.

(40) Lee, M. R.; Bland, P. A. Dating climatic change in hot deserts using desert varnish on meteorite finds. *Earth Planet. Sci. Lett.* **2003**, *206*, 187–198.

(41) Dietzel, M.; Kolmer, H.; Polt, P.; Simic, S. Desert varnish and petroglyphs on sandstone - Geochemical composition and climate changes from Pleistocene to Holocene (Libya). *Chem. Erde* **2008**, *68*, 31–43.

(42) Krinsley, D. Models of rock varnish formation constrained by high resolution transmission electron microscopy. *Sedimentology* **1998**, *45*, 711–725.

(43) Langworthy, K. A.; Krinsley, D. H.; Dorn, R. I. Investigation of Tibetan Plateau Varnish: New Findings at the Nanoscale Using Focused Ion Beam and Transmission Electron Microscopy Techniques. *Scanning* **2011**, *33*, 78–81.

(44) Garvie, L. A.; Burt, D. M.; Buseck, P. R. Nanometer-scale complexity, growth, and diagenesis in desert varnish. *Geology* **2008**, *36*, 215.

(45) Krinsley, D.; Dorn, R. I.; DiGregorio, B. Astrobiological Implications of Rock Varnish in Tibet. *Astrobiology* **2009**, *9*, 551–562.

(46) Dorn, R. I.; Krinsley, D. H.; Langworthy, K. A.; Ditto, J.; Thompson, T. J. The influence of mineral detritus on rock varnish formation. *Aeolian Research* **2013**, *10*, 61–76.

(47) Macholdt, D. S.; Jochum, K. P.; Pöhlker, C.; Stoll, B.; Weis, U.; Weber, B.; Müller, M.; Kappl, M.; Buhre, S.; Kilcoyne, A. L. D.; et al. Microanalytical methods for in-situ high-resolution analysis of rock varnish at the micrometer to nanometer scale. *Chem. Geol.* **2015**, *411*, 57–68.

(48) Macholdt, D. S.; Herrmann, S.; Jochum, K. P.; Kilcoyne, A. L. D.; Laubscher, T.; Pfisterer, J. H.; Pöhlker, C.; Schwager, B.; Weber, B.; Weigand, M.; et al. Black manganese-rich crusts on a Gothic cathedral. *Atmos. Environ.* **2017**, *171*, 205–220.

(49) Macholdt, D. S.; Jochum, K. P.; Pöhlker, C.; Arangio, A.; Förster, J.-D.; Stoll, B.; Weis, U.; Weber, B.; Müller, M.; Kappl, M.; et al. Characterization and differentiation of rock varnish types from different environments by microanalytical techniques. *Chem. Geol.* **2017**, *459*, 91–118.

(50) Maldanis, L.; Hickman-Lewis, K.; Verezhak, M.; Gueriau, P.; Guizar-Sicairos, M.; Jaquetto, P.; Trindade, R. I. F.; Rossi, A. L.; Berenguer, F.; Westall, F.; et al. Nanoscale 3D quantitative imaging of 1.88 Ga Gunflint microfossils reveals novel insights into taphonomic and biogenic characters. *Sci. Rep.* **2020**, *10*, 8163.

(51) De Boever, W. D.; Diaz, A.; Derluyn, H.; De Kock, T. D.; Bultreys, T.; Boone, M.; De Schryver, T. D.; Skjønsvell, E. T. B.; Holler, M.; Breiby, D. W. Characterization of composition and structure of clay minerals in sandstone withptychographic X-ray nanotomography. *Appl. Clay Sci.* **2015**, *7*, 258.

(52) Sharps, M. C.; Grissom, C. A.; Vicenzi, E. P. Nanoscale structure and compositional analysis of manganese oxide coatings on the Smithsonian Castle, Washington, DC. *Chem. Geol.* **2020**, *537*, 119486.

(53) Liu, T.; Broecker, W. S. Holocene rock varnish microstratigraphy and its chronometric application in the drylands of western USA. *Geomorphology* **2007**, *84*, 1–21.

(54) Mayer, J.; Giannuzzi, L.; Kamino, T.; Michael, J. TEM Sample Preparation and Damage. *MRS Bull.* **2007**, *32*, 400–407.

(55) Siemons, W.; Beekman, C.; Fowlkes, J. D.; Balke, N.; Tischler, J. Z.; Xu, R.; Liu, W.; Gonzales, C. M.; Budai, J. D.; Christen, H. M. Focused-ion-beam induced damage in thin films of complex oxide BiFeO<sub>3</sub>. *APL Mater.* **2014**, *2*, 022109.

(56) Krinsley, D.; Ditto, J.; Langworthy, K.; Dorn, R. I.; Thompson, T. Varnish Microlaminations: New Insights from Focused Ion Beam Preparation. *Physical Geography* **2013**, *34*, 159–173.

(57) Kilcoyne, A. L. D.; Tyliczszak, T.; Steele, W. F.; Fakra, S.; Hitchcock, P.; Franck, K.; Anderson, E.; Harteneck, B.; Rightor, E. G.; Mitchell, G. E.; et al. Interferometer-controlled scanning transmission X-ray microscopes at the Advanced Light Source. *J. Synchrotron Radiat.* **2003**, *10*, 125–36.

(58) Follath, R.; Schmidt, J. S.; Weigand, M.; Fauth, K.; Garrett, R.; Gentle, I.; Nugent, K.; Wilkins, S. The X-ray microscopy beamline UE46-PGM2 at BESSY. *AIP Conf. Proc.* **2009**, 323–326.

(59) Weigand, M. Realization of a new Magnetic Scanning X-ray Microscope and Investigation of Landau Structures under Pulsed Field Excitation. Ph.D. thesis, Universität Stuttgart, Stuttgart, 2014.

(60) Dhez, O.; Ade, H.; Urquhart, S. G. Calibrated NEXAFS spectra of some common polymers. *J. Electron Spectrosc. Relat. Phenom.* **2003**, *128*, 85–96.

(61) Urquhart, S. G.; Ade, H.; Rafailovich, M.; Sokolov, J. S.; Zhang, Y. Chemical and vibronic effects in the high-resolution near-edge X-ray absorption fine structure spectra of polystyrene isotopomers. *Chem. Phys. Lett.* **2000**, *322*, 412–418.

(62) Lerotic, M.; Jacobsen, C.; Schäfer, T.; Vogt, S. Cluster analysis of soft X-ray spectromicroscopy data. *Ultramicroscopy* **2004**, *100*, 35–57.

(63) Lerotic, M.; Jacobsen, C.; Gillow, J.; Francis, A.; Wirick, S.; Vogt, S.; Maser, J. Cluster analysis in soft X-ray spectromicroscopy: Finding the patterns in complex specimens. *J. Electron Spectrosc. Relat. Phenom.* **2005**, *144–147*, 1137–1143.

(64) Lerotic, M.; Mak, R.; Wirick, S.; Meirer, F.; Jacobsen, C. MANTiS: a program for the analysis of X-ray spectromicroscopy data. *J. Synchrotron Radiat.* **2014**, *21*, 1206–1212.

(65) Hitchcock, A. P.; Hitchcock, P.; Jacobsen, C.; Zimba, C.; Loo, B.; Rotenberg, E.; Denlinger, J.; Kneedler, R. *aXis 2000—Analysis of X-ray images and spectra* 2018, <http://unicorn.mcmaster.ca/axis/aXis2000-windows-pre-IDL8.3.html> (accessed 2021-10-05).

(66) Schneider, C. A.; Rasband, W. S.; Eliceiri, K. W.; Instrumentation, C. NIH Image to ImageJ: 25 years of Image Analysis. *Nat. Methods* **2012**, *9*, 671–675.

(67) Keskinbora, K.; Grevent, C.; Eigenthaler, U.; Weigand, M.; Schutz, G. Rapid Prototyping of Fresnel Zone Plates via Direct Ga+ Ion Beam Lithography for High-Resolution X-ray Imaging. *ACS Nano* **2013**, *7*, 9788–9797.

(68) Ordavo, I.; Ihle, S.; Arkadiev, V.; Scharf, O.; Soltan, H.; Bjeoumikhov, A.; Bjeoumikhova, S.; Buzanich, G.; Gubzhokov, R.; Gunther, A.; et al. A new pnCCD-based color X-ray camera for fast spatial and energy-resolved measurements. *Nucl. Instrum. Methods Phys. Res., Sect. A* **2011**, *654*, 250–257.

(69) Marchesini, S.; Krishnan, H.; Daurer, B. J.; Shapiro, D. A.; Perciano, T.; Sethian, J. A.; Maia, F. SHARP: a distributed GPU-basedptychographic solver. *J. Appl. Crystallogr.* **2016**, *49*, 1245–1252.

(70) Gilbert, B.; Frazer, B. H.; Belz, A.; Conrad, P. G.; Nealson, K. H.; Haskel, D.; Lang, J. C.; Srajer, G.; De Stasio, G. Multiple scattering calculations of bonding and X-ray absorption spectroscopy of manganese oxides. *J. Phys. Chem. A* **2003**, *107*, 2839–2847.

(71) Pöhlker, C.; Wiedemann, K. T.; Sinha, B.; Shiraiwa, M.; Gunthe, S. S.; Smith, M.; Su, H.; Artaxo, P.; Chen, Q.; Cheng, Y. F.; et al. Biogenic Potassium Salt Particles as Seeds for Secondary Organic Aerosol in the Amazon. *Science* **2012**, *337*, 1075–1078.

(72) Förster, J.-D.; Pöhlker, C. *Dataset for X-Ray Microspectroscopy and Ptychography on Nanoscale Structures in Rock Varnish*; Edmond – the Open Research Data Repository of the Max Planck Society, 2021. DOI: 10.17617/3.7d.

(73) Macholdt, D. S.; Al-Amri, A. M.; Tuffaha, H. T.; Jochum, K. P.; Andreae, M. O. Growth of desert varnish on petroglyphs from Jubbah and Shuwaymis, Ha'il region, Saudi Arabia. *Holocene* **2018**, *28*, 1495–1511.

(74) Gilbert, B.; Frazer, B. H.; Belz, A.; Conrad, P. G.; Nealson, K. H.; Haskel, D.; Lang, J. C.; Srajer, G.; De Stasio, G. Multiple

Scattering Calculations of Bonding and X-ray Absorption Spectroscopy of Manganese Oxides. *J. Phys. Chem. A* **2003**, *107*, 2839–2847.

(75) Pecher, K.; McCubbery, D.; Kneedler, E.; Rothe, J.; Bargar, J.; Meigs, G.; Cox, L.; Nealon, K.; Tonner, B. Quantitative charge state analysis of manganese biominerals in aqueous suspension using scanning transmission X-ray microscopy (STXM). *Geochim. Cosmochim. Acta* **2003**, *67*, 1089–1098.

(76) Tebo, B. M.; Bargar, J. R.; Clement, B. G.; Dick, G. J.; Murray, K. J.; Parker, D.; Verity, R.; Webb, S. M. BIOGENIC MANGANESE OXIDES: Properties and Mechanisms of Formation. *Annu. Rev. Earth Planet. Sci.* **2004**, *32*, 287–328.

(77) Everett, J.; Collingwood, J. F.; Tjendana-Tjhin, V.; Brooks, J.; Lermyte, F.; Plascencia-Villa, G.; Hands-Portman, I.; Dobson, J.; Perry, G.; Telling, N. D. Nanoscale synchrotron X-ray speciation of iron and calcium compounds in amyloid plaque cores from Alzheimer's disease subjects. *Nanoscale* **2018**, *10*, 11782–11796.

(78) van Heel, M.; Schatz, M. Fourier Shell Correlation Threshold Criteria. *J. Struct. Biol.* **2005**, *151*, 250–262.

(79) Herbert, A.; Burri, O. *Fourier Ring Correlation ImageJ Plugin - Commit Sec4783* 2019, <https://github.com/BIOP/ijp-frc> (accessed 2021-10-05).

(80) Nieuwenhuizen, R. P. J.; Lidke, K. A.; Bates, M.; Puig, D. L.; Grünwald, D.; Stallinga, S.; Rieger, B. Measuring Image Resolution in Optical Nanoscopy. *Nat. Methods* **2013**, *10*, 557–562.

#### ■ NOTE ADDED AFTER ASAP PUBLICATION

This paper was published ASAP on October 6, 2021, with an incomplete reference and Figure 3 introduced during production. The corrected version was posted October 7, 2021.